

Direct probing of energy gaps and bandwidth in gate-tunable flat band graphene systems

Received: 30 June 2024

Accepted: 9 January 2025

Published online: 03 February 2025



Jin Jiang¹, Qixuan Gao¹, Zekang Zhou¹, Cheng Shen¹, Mario Di Luca¹, Emily Hajigeorgiou¹, Kenji Watanabe², Takashi Taniguchi² & Mitali Banerjee^{1,4}✉

Moiré systems featuring flat electronic bands exhibit a vast landscape of emergent exotic quantum states, making them one of the resourceful platforms in condensed matter physics. Tuning these systems via twist angle and the electric field greatly enhances our comprehension of their strongly correlated ground states. Here, we report a technique to investigate the nuanced intricacies of band structures in dual-gated multilayer graphene systems. We utilize the Landau levels of a decoupled monolayer graphene to extract the electric field-dependent bilayer graphene charge neutrality point gap. Then, we extend this method to analyze the evolution of the band gap and the flat bandwidth in twisted mono-bilayer graphene. The band gap maximizes at the same displacement field where the flat bandwidth minimizes, concomitant with the emergence of a strongly correlated phase. Moreover, we extract integer and fractional quantum Hall gaps to further demonstrate the strength of this method. Our technique paves the way for improving the understanding of electronic band structures in versatile flat band systems.

Understanding the band structure of a system is of fundamental significance in condensed matter physics. For instance, the linear conical energy spectrum of monolayer graphene (MG) gives rise to two inequivalent K points, which results in the observation of the half-integer quantum Hall effect^{1–3}. A small twist angle between two graphene sheets induces a long-range periodic pattern, resulting in angle-dependent moiré Bloch bands⁴. Particularly, near a “magic angle” (~1.1°) of rotation between the layers, the coupling between two graphene sheets is strongly reinforced, and the low-energy moiré bands become very narrow, almost without any dispersion (flat)⁵. This gives rise to exotic quantum phases, including strongly correlated insulating states^{5–12}, unconventional superconductivity^{9–15}, ferromagnetism^{16–18}, etc.

Due to the flexible carrier density control by dual electrostatic gating, twisted multilayer graphene flat band systems have become an

appealing platform for studying strongly correlated quantum phases. For example, orbital Chern insulators at different integer filling factors were observed in twisted monolayer-bilayer graphene (TMBG)^{19,20}. In contrast, spin-polarized insulating states were observed in twisted double-bilayer graphene (TDBG)^{21–23}, etc.

The dual gate tuning provides a fundamental degree of freedom to understand the rich phases mentioned above. To study these exotic phases, an experimental technique that can accurately measure the response of the device under an applied electric field is crucial. Several single-gated local probe techniques have been developed to enrich the understanding of band structure in two-dimensional materials, like scanning tunneling microscopy/spectroscopy (STM/STS)^{4,8,23–27}, single electron transistor (SET)²⁸, planar tunneling junction²⁹ and nano-SQUID³⁰. In addition to local probes, global measurements, including

¹Laboratory of Quantum Physics (LQP), Institute of Physics, École Polytechnique Fédérale de Lausanne (EPFL), 1015 Lausanne, Switzerland. ²Research Center for Electronic and Optical Materials, National Institute for Materials Science, 1-1 Namiki, Tsukuba 305-0044, Japan. ³Research Center for Materials Nanoarchitectonics, National Institute for Materials Science, 1-1 Namiki, Tsukuba 305-0044, Japan. ⁴Center for Quantum Science and Engineering (QSE Center), École Polytechnique Fédérale de Lausanne (EPFL), 1015 Lausanne, Switzerland. ✉e-mail: mitali.banerjee@epfl.ch

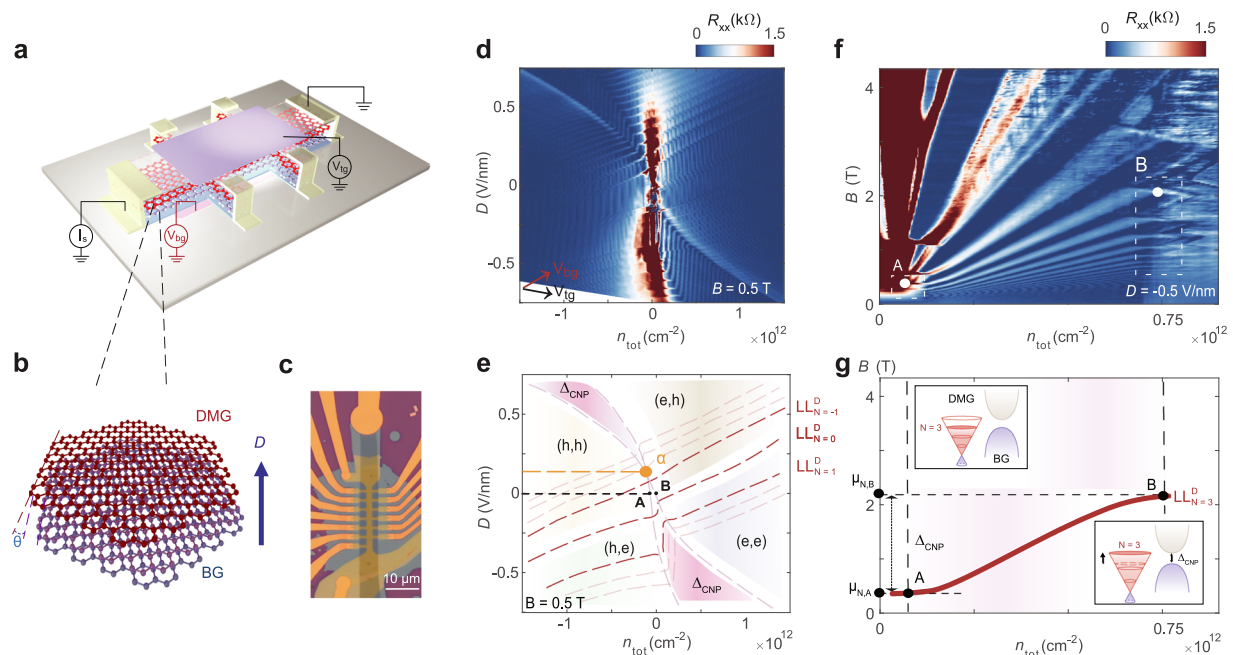


Fig. 1 | Twisted decoupled monolayer graphene (DMG) with bilayer graphene (BG). **a** The schematic of the device and measurement configuration. **b** The schematic of DMG stacked on top of the BG. The blue arrow pointing to the DMG indicates the positive direction of the applied displacement field D . **c** The optical image of the DMG + BG (Device_A1) device. **d** Longitudinal resistance R_{xx} as a function of the total carrier density (n_{tot}) and D at $B = 0.5$ T. The red (black) arrow indicates the direction of the bottom gate (top gate). The Dirac cone of the DMG splits into many Dirac Landau levels along the top gate (V_{tg}) direction. **e** A colored schematic diagram of the main features of n - D mapping in Fig. 1d. Magenta anti-S-shaped region represents the CNP of the BG (Δ_{CNP}). The two boundaries of the CNP gap of the BG are indicated by faint dashed lines intersecting at α , where $D = 0.13$ V/nm. A and B are

edges of the CNP gap of the BG for the same displacement field ($D = 0$ V/nm). A series of Dirac LLs of DMG (red dashed line along the diagonal) shuffle along the top gate direction. LL_N^D is the N th Dirac Landau level of DMG. The letters inside the parentheses represent the carrier types for BG (first) and DMG (second). “e” stands for electrons, and “h” stands for holes. **f** Landau fan diagram of R_{xx} near the CNP of the BG at $D = -0.5$ V/nm. White dots A and B represent the band crossing between the third Dirac LL of the DMG and the CNP of the BG. **g** A schematic diagram of extracting the CNP gap of BG. The insets schematize the third LL of DMG located at the edges of the CNP gap of the BG. The gap is extracted from the change in the chemical potential of LL. The chemical potential is calculated from $\mu_N = \mu_{N=0} + v_F \cdot \sqrt{2ehN \operatorname{sgn}(N)B}$.

magneto-transport^{5–15,19–23}, nano angle-resolved photoemission spectroscopy (Nano-ARPES)^{31,32}, electronic compressibility³³, nano-infrared imaging³⁴, and Fourier transform infrared (FTIR) spectroscopy^{35,36} are widely adopted. However, the limiting factor in most of these aforementioned techniques, like STM/STS and nano-ARPES, is that the samples are designed only with one gate.

Although electronic compressibility measurements, nano-infrared imaging, Nano-SQUID-on-tip microscopy, and FTIR spectroscopy can investigate dual gate devices, these measurements each have their drawbacks^{30–32,34–36}. For example, the large beam spot (~ 1 mm) used in FTIR spectroscopy, compared with the size of typical devices, makes the experiments substantially challenging. While conventional transport measurements for extracting the energy gap, such as resistance vs. temperature (R - T) measurements, have been widely adopted, the thermally activated gap overshadows other details. In addition, this method cannot extract the bandwidth.

Recently, the unique band structure in twisted trilayer graphene has enabled the dissociation of intertwined bands and the quantification of energy gaps¹⁵. Similarly, using decoupled monolayer graphene has facilitated the uncovering of spin ordering in twisted bilayer graphene³⁷. These advancements inspire further investigation into the electronic band structures of electric field-tunable systems, including the direct probing of energy gaps and bandwidths in gate-tunable flat band graphene systems.

Results

Gate-tunable CNP gap in BG

To benchmark our technique, we perform electrical transport measurements on a dual-gated Hall bar fabricated on a monolayer

graphene (MG) stacked on a bilayer graphene (BG) with a large twist angle (see Fig. 1a, b). The calculated band structures of TMBG indicate that a large twist angle ($\theta \geq 10^\circ$) between MG and BG is necessary to effectively decouple the two layers (Supplementary Figs. 1, 2)³⁸.

We trace the CNP of this decoupled MG (DMG), which is denoted by the red dashed line in phase diagrams of Fig. 1d, e, $LL_{N=0}^D$ and N is the Landau level index. In our device configuration, the BG is closer to the bottom gate. Hence, the bottom gate cannot effectively tune the DMG due to the screening from the BG, which is evident from the trace of the CNP line of the DMG as it is almost parallel to the bottom gate direction. Moreover, we observe multiple Landau levels splitting under a finite magnetic field (Supplementary Fig. 3). These Dirac Landau levels of the DMG (LL_N^D) shuffle along the V_{tg} direction when V_{bg} is fixed.

Using Landau level spectroscopy, we estimated the Δ_{CNP} value (see Methods). Since the DMG is decoupled from the BG, we can directly estimate the chemical potential extracted from the LL_N^D . Figure 1f shows the band crossings between the LL_N^D and the CNP edges of the BG denoted by A and B. In order to estimate Δ_{CNP} , we take $LL_{N=3}^D$ (Fig. 1g) as an example. $\mu_{N,A}$, $\mu_{N,B}$ denote chemical potentials of the left and right CNP edges (indicated by two horizontal black dashed lines and inset schematics), following $\mu_N = \mu_{N=0} + v_F \cdot \sqrt{2ehN \operatorname{sgn}(N)B}$, where Fermi velocity $v_F = 1 \times 10^6$ m/s^{35,39–41} and \hbar is the reduced Planck constant. The chemical potential difference $\Delta_N = |\mu_{N,A} - \mu_{N,B}|$ represents the energy gap size of the bilayer graphene CNP.

In Fig. 2a, at both points A and B, the chemical potential extracted through the different LL_N^D changes as \sqrt{B} , implying that A and B both track the same DMG Landau levels. For different LL_N^D , the Δ_{CNP} values remain consistent, with small variation (Fig. 2c).

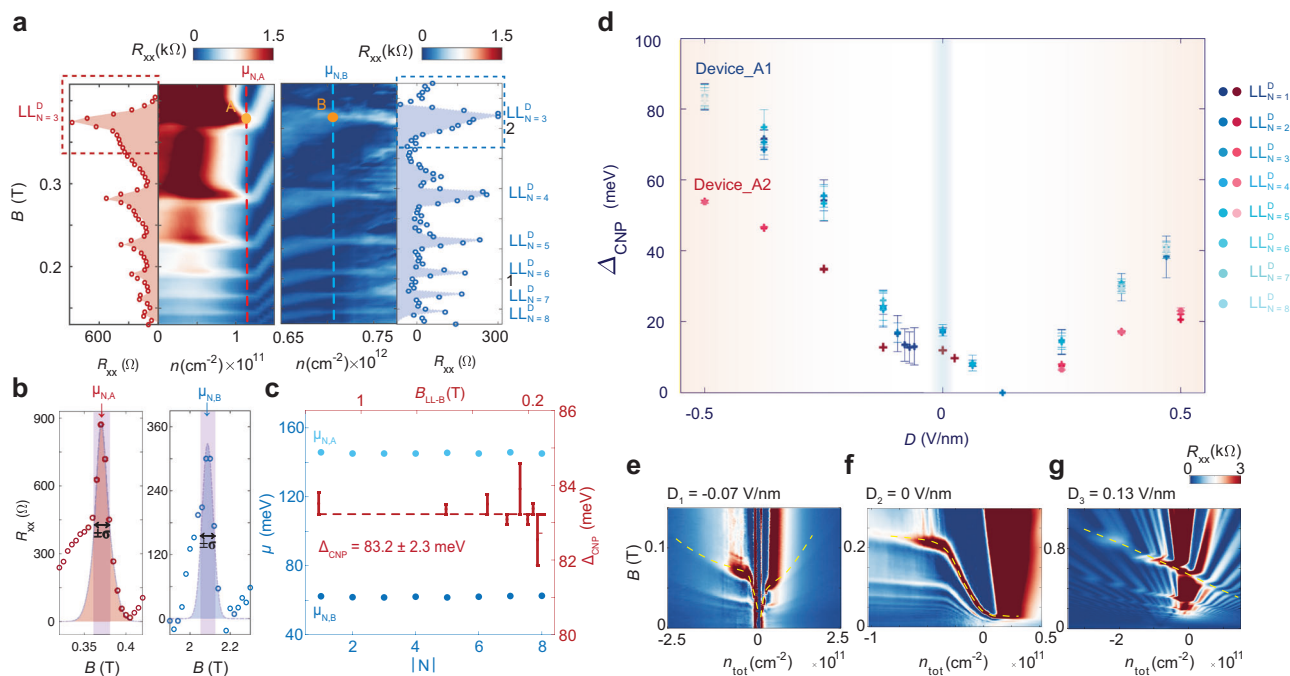


Fig. 2 | Electric field-dependent energy gap extraction from DMG Landau level spectroscopy. **a** Zoom-in Landau fan diagrams of the white dashed rectangular regions in Fig. 1f. Clear Dirac LLs of the DMG are indicated by red and blue dashed lines and LL_N^D . The interval between LLs changes linearly with \sqrt{B} . **b** The error bars of the chemical potential are derived from fitting the full-width half maximum (FWHM) of the high longitudinal resistance R_{xx} peak at points A and B, which are fitted to a Gaussian function. The $\pm\sigma$ are error edges of the corresponding chemical potentials. **c** The CNP gap (Δ_{CNP}) of the BG extracted from different LLs of DMG. Δ_{CNP} is the change of chemical potential along the gap. Since the error bars are

derived from the broadening of Landau levels (LLs), the resolution of the experiments can be improved by using LLs with narrower bandwidths. The top axis B_{LL-B} tracks the magnetic field of point B for every LL with index N . **d** Gap evolution as a function of D for Device_A1 (22°) and Device_A2 (27°). The overlap of blue and red dots demonstrates the consistency of the gap extracted from different LLs, which increases with increasing $|D|$. The difference in Coulomb potential between two layers of BG induces a small gap at zero displacement field. **e–g** Landau Level spectroscopy at different D . The yellow dashed line indicates the kink of the first LL of the DMG. The gap completely closes at a small positive electric field D_3 .

We then extend our analysis to include various displacement fields (D), allowing us to observe the electric field dependence of Δ_{CNP} in BG of two devices (Fig. 2d). The Δ_{CNP} in BG increases significantly with increasing $|D|$ as a result of the difference in Coulomb potential between the layers. The estimated Δ_{CNP} at $D = -0.5$ V/nm is 83.2 ± 2.3 meV of Device_A1, is in agreement with previous findings^{42,43}.

Next, we take Device_A1 as the main device, and we observe a finite built-in gap (17.2 ± 1.3 meV) at the CNP at $D = 0$ V/nm, which results from layer polarization of the valence and conduction bands^{44,45}. Furthermore, we observe the evolution of the CNP gap closing and reopening with increasing positive D (Fig. 2e–g and Supplementary Figs. 4–6). Particularly, at $D_3 = 0.13$ V/nm, the gap is completely closed by a sign change of Coulomb potential difference⁴⁶, which is indicated by the α point in Fig. 1e. This behavior results from the asymmetric response of the displacement field and layer polarization. The weaker response of the CNP gap at positive D (pointing to MG, $D = 0.25$ V/nm, Δ_{CNP} is 14.3 ± 2.7 meV) compared to negative D (pointing to BG, $D = -0.25$ V/nm, Δ_{CNP} is 55.3 ± 4.0 meV) supports this observation. In addition, we observe that the CNP gap does not fully close within the moderate negative D range (D_2 to D_1). Further investigation is needed into the band structure, particularly considering the overlap between the CNP of the DMG and the BG.

Bandwidth and bandgap of TMBG

To establish the robustness of this technique, we study a more complicated electric field-tunable flat band system-TMBG. The DMG was placed on top of the monolayer graphene of the small twist angle TMGB ($1.14^\circ \pm 0.02^\circ$) (Fig. 3a). The schematic compares the moiré patterns of TMGB and DMG+TMGB, the moiré length is equal to

~ 13 nm, and does not change significantly with the addition of the DMG. A n - D map at $B = 1$ T is shown in Fig. 3d (Supplementary Fig. 7). We observe similar multiple Landau levels LL_N^D splitting as in Fig. 1d. Then the strongly correlated states are observed at all integer filling factors and are found to vary with the D .

Figure 3f shows the extracted flat bandwidth and bandgap as a function of D (see Methods and Supplementary Figs. 8–14). When the correlated state appears at the same D as point α ($D = 0.33$ V/nm) with filling factor 3, the flat bandwidth is estimated to be about 73.5 ± 1.8 meV, which is in good agreement with the experimental work in TMGB (70 ± 10 meV)⁴⁷. Furthermore, due to the narrow width of the LL_N^D (Fig. 2a), the experimental error is smaller (< 1 meV) than the reported values, showcasing the high precision of this method. From point α to point β ($D = 0.53$ V/nm), the flat bandwidth decreases to 64.5 ± 0.6 meV as D increases, which shows that D greatly suppresses the width of the flat band. Simultaneously, the bandgap varies inversely with the D . Particularly, at point β , the flat bandwidth reaches a minimum while the bandgap maximizes, and a correlated state appears at filling factor $\nu = 1$ (Fig. 3e). This might be explained by the fact that the strongest correlation occurs where the flat band is at a minimum, which is accompanied by the weakest correlated insulator at $\nu = 1$. However, it is not true that strong electron-electron interactions can lead to counterintuitive effects, such as an enhancement in the bandwidth. Specifically, the effective potential landscape that the carriers experience could induce fluctuations, resulting in a broadening of the bandwidth. Despite this, by extracting the bandwidth at the exact points where correlated states are generated, we can observe how the bandwidth varies with the occurring states and extract the energy change in the bandwidth corresponding to the correlation where two correlated states transform. This provides valuable insights

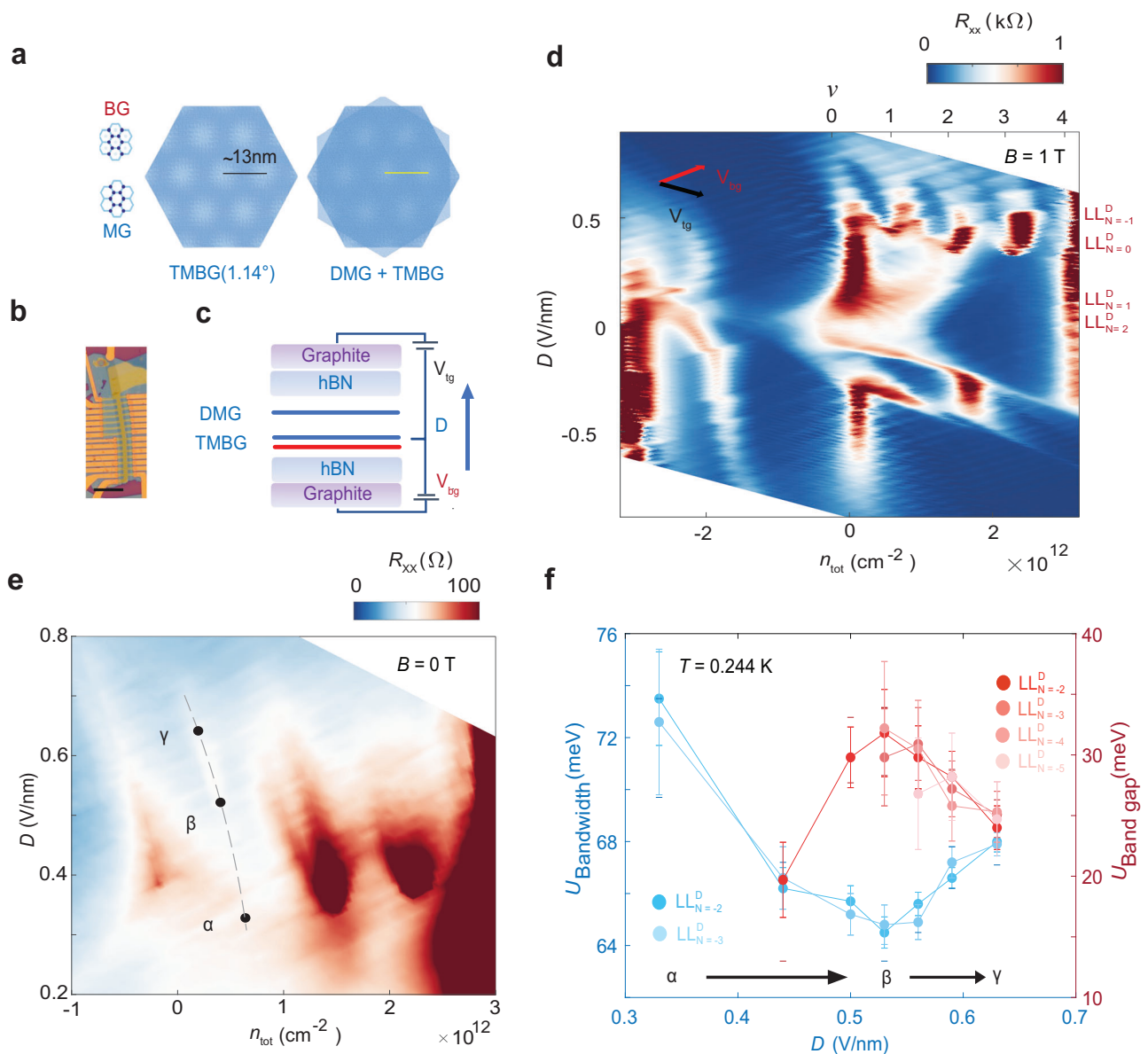


Fig. 3 | Evolution of bandwidth and bandgap with displacement field in twisted mono-bilayer graphene. **a** Schematics of TMBG and DMG with TMBG. The left panel is a moiré pattern of the TMBG ($1.14^\circ \pm 0.02^\circ$). The right panel is DMG on top of the TMBG, indicating the same moiré length as TMBG. **b** Optical image of Device_B3. The black scale bar is $10\text{ }\mu\text{m}$. **c** The configuration of dual gate measurements. The blue arrow pointing to the DMG indicates the positive direction of the applied displacement field D . **d** R_{xx} as a function of the n_{tot} and D at $B = 1\text{ T}$. The

asymmetric phase dependent on D is similar to a phase of pure TMBG, indicating that the monolayer graphene is fully decoupled from BG. The correlated states appear at all integer filling factors at positive D . **e** Zoom-in of the n - D map presented in Fig. 3d, at $B = 0\text{ T}$. **f** The TMBG flat bandwidth and bandgap evolution at different D . The minimum of the bandwidth and the maximum of the bandgap at $D = 0.53\text{ V/nm}$ (β), where exactly the $\nu = 1$ correlated state emerges in Fig. 3e.

into the model and parameters of correlation, which will help refine future studies. From β to γ , the flat bandwidth broadens with increasing D and decreasing bandgap, reflecting weaker electronic correlations. According to the previous works^{19,20}, the flat band gradually touches the remote dispersive band as D increases.

For TMBG, the spatial inversion symmetry is broken; and it exhibits a rich phase diagram similar to the one of twisted bilayer graphene (TBG) when a D is applied in the direction of MG (TMBG side). The TMBG also exhibits a phase diagram similar to that of twisted double-bilayer graphene (TDBG) when the D is inverted^{19,20}.

Thus, in addition to the four DMG/TMBG devices (Supplementary Fig. 7), where the DMG was placed approximately on the monolayer graphene side of the TMBG, in contrast, for Device_B5, the DMG was placed on the bilayer graphene side of the TMBG (Supplementary

Fig. 15). When carriers are pushed toward the monolayer graphene side of TMBG under positive (negative) displacement fields, the gap in Device_B5 opens larger than in Device_B3, highlighting the screening effect from the DMG (Supplementary Figs. 16, 17). This provides a robust experimental method to support theoretical efforts in understanding the complex phase diagrams of these multilayer graphene systems in the future.

Integer and fractional quantum Hall gaps

To further warrant the accuracy of this technique, we demonstrate how this method can be used to extract integer and fractional quantum Hall gaps for the TMBG flat band. The four-fold degeneracy of LLs for both DMG and the flat band is lifted (Supplementary Figs. 8–10). In Fig. 4a, we clearly see four mini-bands LL_l^D formed from $LL_{N=-1}^D$

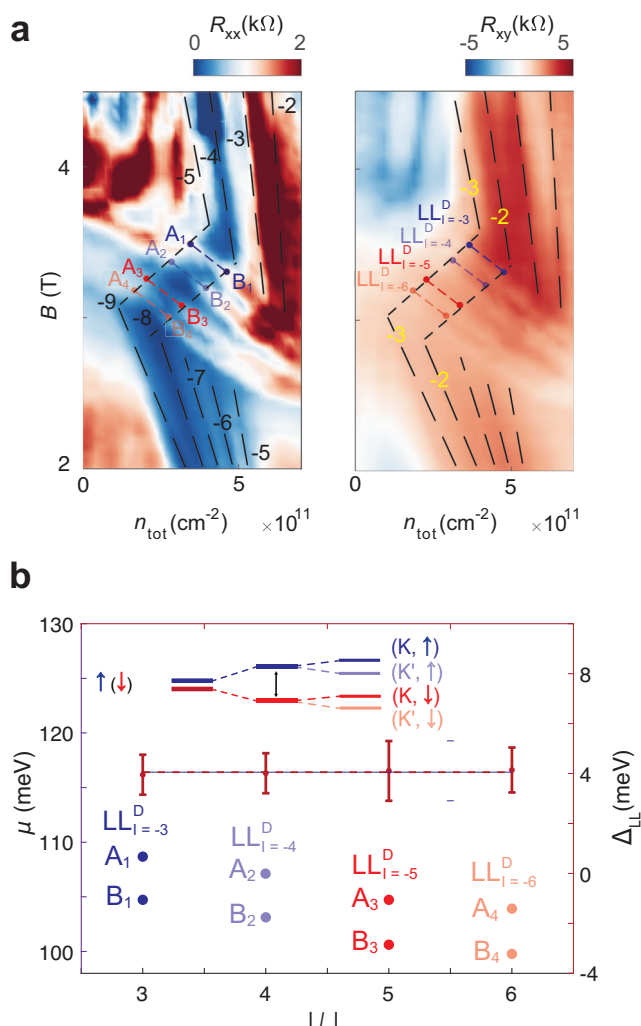


Fig. 4 | Flat-band integer Landau level gap. **a** Longitudinal resistance R_{xx} and Hall resistance R_{xy} as a function of n_{tot} and B . The Dirac LLs degeneracy is lifted, and $LL_{N=-1}^D$ splits into four mini-bands $LL_{l=-3}^D$ indicated by the purple and red dashed lines. The black dashed lines indicate the flat band LLs. As DMG LLs offer Chern number offset, the corresponding Chern number C (indicated by black number) equals C_f (indicated by yellow number) + C_D , C_f and C_D are Chern numbers of the TMBG flat band and DMG Dirac band respectively. **b** The flat band integer Landau level gap ($LL_{l=-2}^f$). Multiple As, Bs represent gap edges of $LL_{l=-2}^f$ and the estimated gap $\Delta_N = |\mu_A - \mu_B| = 4.1 \pm 0.9 \text{ meV}$ is averaged through different $LL_{l=-2}^f$.

splitting, indicated by red and purple dashed lines. These DMG Landau levels with different filling factors induce additional Chern number offsets ($-l$) (Supplementary Figs. 18–20). The total Chern number C (indicated by the black numbers) is the summation of C_f (indicated by the yellow numbers) and C_D , where C_f and C_D are Chern numbers of the TMBG flat band and DMG Dirac band, respectively. Multiple As and Bs represent gap edges of $LL_{l=-2}^f$ and the estimated gap $\Delta_N = |\mu_A - \mu_B|$ is averaged through different $LL_{l=-2}^f$ (Fig. 4b). The extracted values of the gap measured by different LLs are consistent with each other, and the average value of the gap is given by $4.1 \pm 0.9 \text{ meV}$.

We extend a similar analysis to a fractional quantum hall gap. Figure 5a, b show R_{xx} and R_{xy} as a function of B and n_{tot} near the CNP region. The schematic of the corresponding Landau level crossings is shown in Fig. 5c. The $N=-1$ Dirac Landau level splits into four mini bands, indicated by the green (Landau level filling factor $l=-3$), blue ($l=-4$), purple ($l=-5$), and pink ($l=-6$) lines, respectively. Thus, the Chern number cascade was observed when crossed with the flat band

Landau levels. Figure 5d exhibits near zero R_{xx} (blue line) and corresponding well-quantized R_{xy} plateaus (red line); these are line cuts taken along the blue and red dash line in Fig. 5a, b. A difference of neighboring LL_N^D filling factor is one, indicating that the degeneracy of the system is fully lifted.

According to the band edges A and B shown in Fig. 5e, a fractional quantum hall gap can be extracted from the band crossing between the fractional quantum hall flat band $\nu_f = -6 + 1/3$ and the Dirac band $LL_{l=-5}^D$ ($C_D = -5$). The magnetic fields in Fig. 5e at A and B are 4.310 ± 0.005 and 4.270 ± 0.005 T, respectively. Thus, the extracted flat band fractional quantum hall gap is $\Delta_N = |\mu_A - \mu_B| = 0.56 \pm 0.14 \text{ meV}$ at around 4.3 T. At filling factors $\nu = -11$ and $\nu = -11 + 1/3$, R_{xx} exhibits a minimum (blue line), while R_{xy} shows a kink (red line), as illustrated in Fig. 5f. This guides us to define the edges of the FQHE in Fig. 5e. Our fractional quantum hall gap results are comparable to results from the reported studies, which yielded $\Delta_{1/3} \sim 1.4$ to 1.8 meV at 12 T ^{48–51}.

In comparison with the conventional R -Tactivation method, the $\nu = 1/3$ fractional quantum Hall gap for two devices in GaAs quantum wells is reported as (8.7 ± 0.1) and $(8.0 \pm 0.4) \text{ K}$ ^{52,53}, corresponding to 0.69 and 0.75 meV , respectively. In graphene, the $\nu = 1/3$ plateau persists up to $T \sim 10 \text{ K}$, equivalent to 0.86 meV ^{54,55}. Particularly, the fractional quantum hall gaps for LLs with higher filling factor is smaller than normal $\nu = 1/3$ ($< 10 \text{ K}$, 0.86 meV)⁵¹. These results are quite comparable to our data, where the extracted fractional quantum hall gap is $0.56 \pm 0.14 \text{ meV}$ at around 4.3 T.

To summarize, we have used the Landau levels of decoupled monolayer graphene to measure the chemical potential of dual-gated multilayer graphene devices. We measured the electric field-tunable CNP gap of bilayer graphene. Then, we extracted the electric field-tunable flat bandwidth and bandgap in twisted mono-bilayer graphene. Moreover, the measurements of the flat band integer and fractional quantum Hall gaps provide a promising avenue to investigate nuanced band structure.

This technique has far-reaching consequences for studying strongly correlated states^{37,56,57}. For example, the superconducting phase diagram and the ground state can be understood by studying adjacent correlated states (Supplementary Fig. 21). Currently, there is a scarcity of techniques that establish a connection between the displacement field-tunable flat bandwidth and strong electron-electron correlations. Our work can encourage more theoretical works to understand the complicated phase diagrams of these multilayer graphene systems. Furthermore, it could be extended in the future to other similar moiré systems, such as transition metal dichalcogenides systems.

Methods

Device fabrication

The devices are fabricated using an advanced technique known as “cut and stack”¹². Pristine materials such as monolayer graphene, bilayer graphene, hBN (10–50 nm), and graphite flakes (3–15 nm) were mechanically exfoliated on an oxygen plasma-etched SiO_2 (285 nm) surface. Next, we used atomic force microscopes (AFM) to pre-cut monolayer graphene and bilayer graphene. High-quality homogeneous poly (bisphenol A carbonate) (PC)/polydimethylsiloxane (PDMS) was then stacked on the glass slide used to transfer the 2D materials flakes to the alignment marker chip. The transfer stage precisely controls the twisted angle between two 2D materials to within 0.1° resolution. The graphite top gate is then fabricated, followed by the electrodes by electron beam lithography and metal evaporation. Here, we use the conventional etching method to define Hall bars. We etch graphite and hBN with O_2 and SF_6 gases, respectively. Optimization of the etching parameters is important to obtain 1D edge contacts with the Cr/Au (5/50 nm) electrodes⁵⁸.

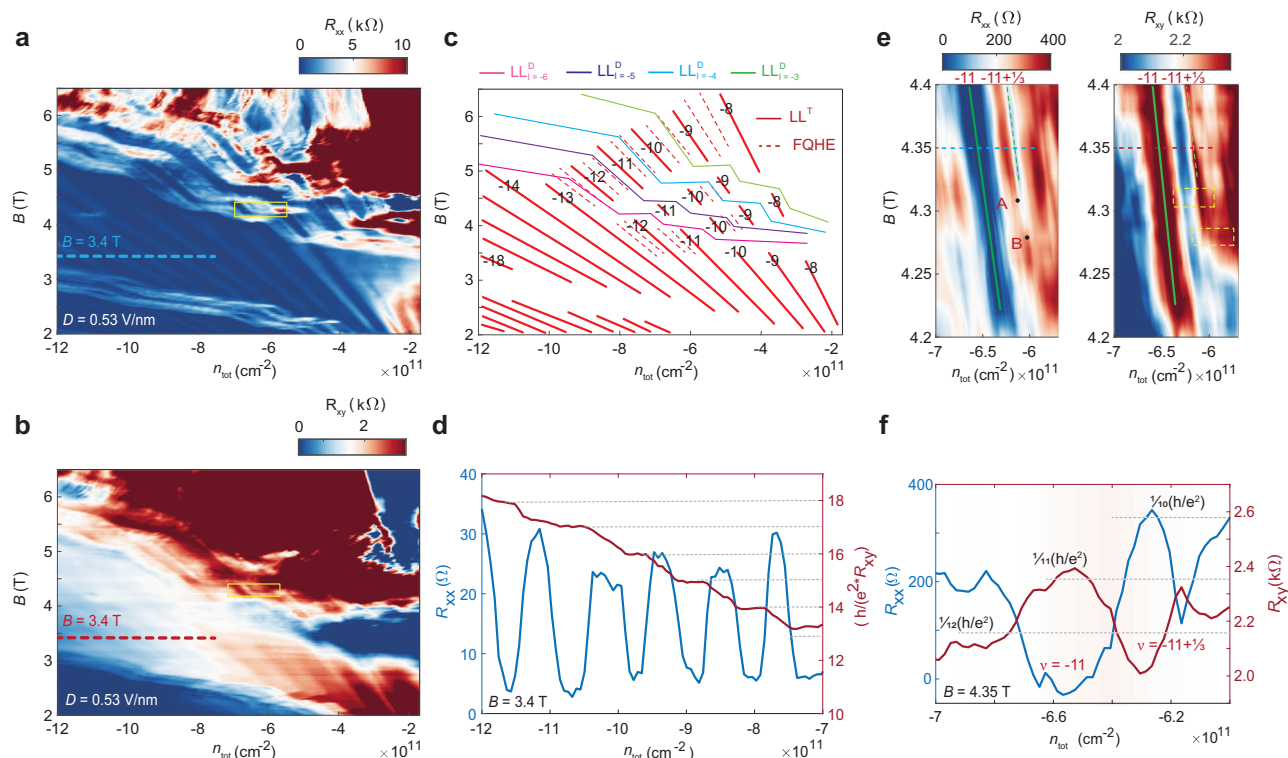


Fig. 5 | Chern number cascade and fractional quantum Hall gaps.

a, b Longitudinal resistance R_{xx} and Hall resistance R_{xy} as a function of n_{tot} and B . **c** Schematic of quantum oscillation of Fig. 5a. LL^T is TMBG flat band LLs composed with DMG LLs Chern number offset. **d** Filling factor dependence of longitudinal resistance (blue dash line in Fig. 5a) and Hall resistance plateaus (red dash line in Fig. 5b). **e** zoomed Landau fan taken from yellow rectangular in Fig. 5a, b. The solid

green line indicates $\nu = -11$ integer quantum Hall state. The green dashed line denotes a fractional quantum Hall state of $\nu_f = -6 + 1/3$. A, B are band edges of the fractional quantum Hall gap of $\nu_f = -6 + 1/3$. The estimated gap $\Delta_N = |\mu_A - \mu_B| = 0.56 \pm 0.14$ meV. **f** Evidence of a fractional quantum Hall state. The data of R_{xx} and R_{xy} are taken along the blue and red dash lines in Fig. 5a, b.

Measurements

Transport measurements were conducted in the cryostat (Oxford Instruments, Heliux), with a base temperature of ~ 275 mK. Standard lock-in techniques were employed using the Stanford Research SR860, with an excitation frequency of $f = 17.7777$ Hz and an AC excitation current (I_s) of less than 10 nA to avoid sample heating and minimize bias effects, we used NF voltage pre-amplifiers with an impedance of 100 MΩ before feeding signals into the lock-in amplifiers (Stanford Research SR860). The transport measurements are conducted in a four-terminal geometry. The device was biased along the major axis of the Hall bar to ensure a uniform current flow, while both longitudinal and transverse voltage drops were simultaneously recorded. Gate voltages were applied using source meters (Yokogawa GS100), and an additional global gate was implemented to enhance the contact quality. We can extract n_{tot} and the displacement field D using the following equation $n_{\text{tot}} = V_{\text{bg}}C_{\text{bg}}/e + V_{\text{tg}}C_{\text{tg}}/e$, $D = |V_{\text{bg}}C_{\text{bg}} - V_{\text{tg}}C_{\text{tg}}|/(2\epsilon_0)$. C_{bg} and C_{tg} are the capacitances between the top (V_{tg}) and bottom (V_{bg}) gates and the DMG + TMBG, e is the electron charge, and ϵ_0 is the vacuum permittivity.

Twisted angle determination

Due to the decoupling of the DMG from the TMBG, the carrier density $n_{\text{flat-band}}$ observed by $\nu = \pm 4 \pm n_s$ of band insulating states. This value can be determined by analyzing quantum oscillations in the Landau fan diagram or by making observations in an n - D diagram. n as a function of the twisted angle following equation $n_s = 8\theta^2/\sqrt{3}a^2$ determines twisted angle of our TMBG ($1.14^\circ \pm 0.02^\circ$), $a = 0.246$ nm is the lattice constant of graphene. The same rule applies to determining small-angle TMBG.

Extracting the gaps and bandwidths

We focus on the CNP gap of BG to demonstrate the method of extracting the energy scale of gaps and bandwidths. By measuring the chemical potential jump across at the intersections between Dirac Landau levels (LLs) and the CNP gap, the chemical potentials at the two edges of the CNP can be determined by: $\mu_N = \mu_{N=0} + v_F \cdot \sqrt{2ehN \text{sgn}(N)B}$ as mentioned in the main text. The Fermi velocity (v_F) remains nearly constant with respect to the Landau level index (N), magnetic field (B), large twist angle ($\theta > 10^\circ$), and intermediate displacement field (D)^{15,39–41}, where the Fermi velocity $v_F = 1 \times 10^6$ m/s and \hbar is reduced Planck constant. The steps involved in this observation are outlined below:

- Identify the gap edge of BG. Since in the gap of BLG, there's no DOS, and the charging electrons will accumulate in LL of DMG shown in Fig. 1f, g. We obtain the exact CNP gap edge points A and B for every LL index N by tracking the crossing state that corresponds to partial filling of Dirac LLs at the Fermi level, which is marked by an R_{xx} peak, indicating the edge of incompressible gaps of Dirac LLs. The R_{xx} peak represents a general mark of extracting the energy scale without considering the lifting of LLs degeneracy. This process is illustrated by the red dashed line and the blue dashed line in the top panel, Region I, of Supplementary Fig. 8c and the right panel of Supplementary Fig. 9c.
- Identify the Landau level index of DMG.
- To determine the magnetic field corresponding to the CNP gap edge points A and B at the gap boundary, we refer to Fig. 1f and g. The magnetic field dictates the chemical potential at each point for a given N th Landau level (LL). By fitting the high-

resistance states R_{xx} peak at the gap edge, we extracted the values of B_1 and B_2 along with their respective uncertainties (σ). Owing to the exceptional quality of our devices, these measurements offer remarkably high energy resolution.

- (iv) Using formula $\mu_N = \mu_{N=0} + v_F \cdot \sqrt{2ehN \operatorname{sgn}(N)B}$ to extract the chemical potential of the edges and then get the CNP gap value.

We observed that the degeneracy of Landau levels (LLs) is lifted by applying higher magnetic fields, altering the energy spectrum of massless Dirac fermions. Consequently, we introduce a generalized energy spectrum for graphene Landau levels that incorporates the effects of degeneracy lifting, such as Zeeman splitting and valley polarization.

The modified equation is shown as below, $E_{N,s,\sigma} = v_F \sqrt{2eh|N|B} + \frac{1}{2}g_s\mu_BBs + \Delta_\sigma K^{3,41,59-61}$, where N is Landau level index, \hbar is Reduced Planck constant, g_s is spin g-factor (typically ~ 2 in graphene), μ_B is Bohr magneton, s is the spin state (+1 for up, -1 for down), Δ_σ is Valley splitting energy, representing energy differences between the K and K' valleys, K is Valley index (± 1).

The degeneracy-lifted sub-LLs create incompressible Landau level gaps in the partially filled Dirac LLs, as observed in the original R_{xx} peak (Supplementary Figs. 8, 9). In Supplementary Fig. 8c, from region I to III, we track the crossing state at point A₁, which corresponds to the crossing between the lowest incompressible degeneracy-lifted Dirac sub-LL ($l = -6$) and the flat band edge. This crossing is marked by a minimum in R_{xx} and corresponding kinks in R_{xy} (Supplementary Fig. 8d, e). A similar rule is applied to the isospin-polarized Dirac LLs ($LL_{N=-2}^I, A_2$). Further details can be found in Supplementary Fig. 9.

The errors in the energy extraction of gaps or bandwidths arise from three main factors:

- (i) The broadening of Landau levels.

It plays a crucial role in determining the accuracy of energy extraction for gaps or bandwidths. This broadening can result from several factors, including disorder, random strain fields, temperature effects, electron-phonon coupling, and many-body interactions. To achieve a narrower bandwidth for Dirac LLs and reduce these errors, it is essential to use clean and uniform samples.

- (ii) Zeeman splitting, isospin-polarized sub-LLs, and fully-degeneracy lifting sub-LLs.

As the magnetic field increases, the Zeeman splitting effect and the lifting of LL degeneracy become significant and should not be neglected. To accurately extract the chemical potential from the LL spectrum of Dirac fermions, it is necessary to modify the spectrum equation, as shown above.

For the Zeeman splitting term^{59,60}, $\frac{1}{2}g_s\mu_BBs$, using two points at different magnetic fields can introduce some errors. However, this term is relatively small compared to the gaps or bandwidths we measure. For instance, for a change of 1 T magnetic field, the contribution from pure Zeeman splitting to Dirac LLs is approximately $1 \mu_B B \sim 0.058 \text{ meV} (-0.67 \text{ K})$ ⁵⁹, which is negligible in comparison to the CNP gap and bandwidth observed in the main text.

For measuring the fractional quantum Hall gap, the magnetic fields at points A and B in Fig. 5e are 4.310 ± 0.005 and 4.270 ± 0.005 T, respectively. The 0.04 T difference in magnetic field results in a pure Zeeman splitting contribution of $0.04 \times 0.058 \text{ meV} = 0.002 \text{ meV}$, which is much smaller than the gap we measured ($0.56 \pm 0.14 \text{ meV}$). Therefore, we neglected the Zeeman splitting term in the main text for the decoupled system when measuring the chemical potentials at the two edge points under different magnetic fields.

At high magnetic fields, the Dirac LLs split into two isospin-polarized sub-LLs or four fully lifted degeneracy LLs, as described by the LL filling factor l . To minimize the effects of this splitting, we track the crossings between the lowest incompressible, degeneracy-lifted

Dirac sub-LLs ($l = -4$) and the target state. These crossings are marked by a minimum in R_{xx} and corresponding kinks in R_{xy} , (Supplementary Figs. 8d, 9, 10f)

In Supplementary Fig. 9, we specifically discuss the influence on bandgap extraction from two different Dirac LLs: The left panel of the normal case and the right panel for the isospin-polarized case. We found that the difference in the bandwidth extracted for both cases is small, and we averaged the results to reduce errors.

- (iii) Valley splitting

We notice that the energy separation between the Dirac LLs of two sub-LLs (l) is significantly different. In Supplementary Fig. 10d, we clearly observe the A₁ and A₂ sub-LLs of $l = -6, -4$, with a substantial magnetic field separation ($B_{A2} - B_{A1} = 0.5 \text{ T}$). In contrast, at point B, this separation is much smaller, making it difficult to clearly differentiate between the sub-LLs. This suggests that the observed effects might arise from valley splitting. See more discussion in Supplementary Fig. 10.

We must acknowledge that the valley effect cannot be completely ignored, and further theoretical work is needed to incorporate the valley splitting term into the modification of the Dirac fermion LL spectrum.

We should also note that our technique is particularly suitable for detecting systems whose band structures are not highly sensitive to magnetic fields. A useful approach is to focus on higher-index LLs, as this enables the measurement of the chemical potential at lower magnetic fields, where Landau level splitting is not yet significant. Additionally, from Fig. 2a, we observe that the bandwidth at low magnetic fields is narrow, which provides higher resolution with reduced effects from both Zeeman splitting and valley splitting.

Data availability

Source data for all the main figures are available at <https://zenodo.org/records/14585126>. All other data that support the findings of this study are available from the corresponding author upon request.

Code availability

The source codes used to perform the calculations in this paper are available from the corresponding author upon request.

References

- Novoselov, K. S. et al. Two-dimensional gas of massless Dirac fermions in graphene. *Nature* **438**, 197–200 (2005).
- Zhang, Y., Tan, Y.-W., Stormer, H. L. & Kim, P. Experimental observation of the quantum Hall effect and Berry's phase in graphene. *Nature* **438**, 201–204 (2005).
- Zhang, Y. et al. Landau-level splitting in graphene in high magnetic fields. *Phys. Rev. Lett.* **96**, 136806 (2006).
- Yan, W. et al. Angle-dependent van Hove singularities in a slightly twisted graphene bilayer. *Phys. Rev. Lett.* **109**, 126801 (2012).
- Cao, Y. et al. Correlated insulator behaviour at half-filling in magic-angle graphene superlattices. *Nature* **556**, 80–84 (2018).
- Liu, X. et al. Tuning electron correlation in magic-angle twisted bilayer graphene using Coulomb screening. *Science* **371**, 1261–1265 (2021).
- Park, J. M., Cao, Y., Watanabe, K., Taniguchi, T. & Jarillo-Herrero, P. Flavour Hund's coupling, Chern gaps and charge diffusivity in moiré graphene. *Nature* **592**, 43–48 (2021).
- Xie, Y. et al. Spectroscopic signatures of many-body correlations in magic-angle twisted bilayer graphene. *Nature* **572**, 101–105 (2019).
- Yankowitz, M. et al. Tuning superconductivity in twisted bilayer graphene. *Science* **363**, 1059–1064 (2019).
- Lu, X. et al. Superconductors, orbital magnets and correlated states in magic-angle bilayer graphene. *Nature* **574**, 653–657 (2019).

11. Stepanov, P. et al. Untying the insulating and superconducting orders in magic-angle graphene. *Nature* **583**, 375–378 (2020).
12. Saito, Y., Ge, J., Watanabe, K., Taniguchi, T. & Young, A. F. Independent superconductors and correlated insulators in twisted bilayer graphene. *Nat. Phys.* **16**, 926–930 (2020).
13. Cao, Y. et al. Unconventional superconductivity in magic-angle graphene superlattices. *Nature* **556**, 43–50 (2018).
14. Arora, H. S. et al. Superconductivity in metallic twisted bilayer graphene stabilized by WSe₂. *Nature* **583**, 379–384 (2020).
15. Shen, C. et al. Dirac spectroscopy of strongly correlated phases in twisted trilayer graphene. *Nat. Mater.* **22**, 316–321 (2023).
16. Sharpe, A. L. et al. Emergent ferromagnetism near three-quarters filling in twisted bilayer graphene. *Science* **365**, 605–608 (2019).
17. Serlin, C. L. et al. Intrinsic quantized anomalous Hall effect in a moiré heterostructure. *Science* **367**, 900–903 (2020).
18. Nuckolls, K. P. et al. Strongly correlated Chern insulators in magic-angle twisted bilayer graphene. *Nature* **588**, 610–615 (2020).
19. Chen, S. et al. Electrically tunable correlated and topological states in twisted monolayer–bilayer graphene. *Nat. Phys.* **17**, 374–380 (2021).
20. Polshyn, H. et al. Electrical switching of magnetic order in an orbital Chern insulator. *Nature* **588**, 66–70 (2020).
21. Liu, X. et al. Tunable spin-polarized correlated states in twisted double bilayer graphene. *Nature* **583**, 221–225 (2020).
22. Cao, Y. et al. Tunable correlated states and spin-polarized phases in twisted bilayer–bilayer graphene. *Nature* **583**, 215–220 (2020).
23. Shen, C. et al. Correlated states in twisted double bilayer graphene. *Nat. Phys.* **16**, 520–525 (2020).
24. Wong, D. et al. Cascade of electronic transitions in magic-angle twisted bilayer graphene. *Nature* **582**, 198–202 (2020).
25. Jiang, Y. et al. Charge order and broken rotational symmetry in magic-angle twisted bilayer graphene. *Nature* **573**, 91–95 (2019).
26. Choi, Y. et al. Electronic correlations in twisted bilayer graphene near the magic angle. *Nat. Phys.* **15**, 1174–1180 (2019).
27. Kerelsky, A. et al. Maximized electron interactions at the magic angle in twisted bilayer graphene. *Nature* **572**, 95–100 (2019).
28. Zondiner, U. et al. Cascade of phase transitions and Dirac revivals in magic-angle graphene. *Nature* **582**, 203–208 (2020).
29. Tilak, N. et al. Flat band carrier confinement in magic-angle twisted bilayer graphene. *Nat. Commun.* **12**, 1–7 (2021).
30. Uri, A. et al. Mapping the twist-angle disorder and Landau levels in magic-angle graphene. *Nature* **581**, 47–52 (2020).
31. Lisi, S. et al. Observation of flat bands in twisted bilayer graphene. *Nat. Phys.* **17**, 189–193 (2021).
32. Utama, M. I. B. et al. Visualization of the flat electronic band in twisted bilayer graphene near the magic angle twist. *Nat. Phys.* **17**, 184–188 (2021).
33. Tomarken, S. L. et al. Electronic compressibility of magic-angle graphene superlattices. *Phys. Rev. Lett.* **123**, 046601 (2019).
34. Hu, F. et al. Real-space imaging of the tailored plasmons in twisted bilayer graphene. *Phys. Rev. Lett.* **119**, 247402 (2017).
35. Ju, L. et al. Tunable excitons in bilayer graphene. *Science* **358**, 907–910 (2017).
36. Yang, J. et al. Spectroscopy signatures of electron correlations in a trilayer graphene/hBN moiré superlattice. *Science* **375**, 1295–1299 (2022).
37. Hoke, J. C. et al. Uncovering the spin ordering in magic-angle graphene via edge state equilibration. *Nat. Commun.* **15**, 1–7 (2024).
38. Wu, Q., Zhang, S., Song, H.-F., Troyer, M. & Soluyanov, A. A. WannierTools: an open-source software package for novel topological materials. *Comput. Phys. Commun.* **224**, 405–416 (2018).
39. Luican, A. et al. Single-layer behavior and its breakdown in twisted graphene layers. *Phys. Rev. Lett.* **106**, 126802 (2011).
40. Li, G. & Andrei, E. Y. Observation of Landau levels of Dirac fermions in graphite. *Nat. Phys.* **3**, 623–627 (2007).
41. Taychatanapat, T., Watanabe, K., Taniguchi, T. & Jarillo-Herrero, P. Quantum Hall effect and Landau-level crossing of Dirac fermions in trilayer graphene. *Nat. Phys.* **7**, 621–625 (2011).
42. Zhang, Y. et al. Direct observation of a widely tunable bandgap in bilayer graphene. *Nature* **459**, 820–823 (2009).
43. Iwasaki, T., Morita, Y., Watanabe, K. & Taniguchi, T. Dual-gated hBN/bilayer-graphene superlattices and the transitions between the insulating phases at the charge neutrality point. *Phys. Rev. B* **106**, 165134 (2022).
44. McCann, E. Asymmetry gap in the electronic band structure of bilayer graphene. *Phys. Rev. B* **74**, 161403 (2006).
45. McCann, E., Abergel, D. S. L. & Fal'ko, V. I. Electrons in bilayer graphene. *Solid State Commun.* **143**, 110–115 (2007).
46. Ohta, T., Bostwick, A., Seyller, T., Horn, K. & Rotenberg, E. Controlling the electronic structure of bilayer graphene. *Science* **313**, 951–954 (2006).
47. Zhang, H. et al. Observation of dichotomic field-tunable electronic structure in twisted monolayer–bilayer graphene. *Nat. Commun.* **15**, 1–7 (2024).
48. Feldman, B. E., Krauss, B., Smet, J. H. & Yacoby, A. Unconventional sequence of fractional quantum Hall states in suspended graphene. *Science* **337**, 1196–1199 (2012).
49. Shi, Y. et al. Energy gaps and layer polarization of integer and fractional quantum Hall states in bilayer graphene. *Phys. Rev. Lett.* **116**, 056601 (2016).
50. Ghahari, F., Zhao, Y., Cadden-Zimansky, P., Bolotin, K. & Kim, P. Measurement of the $\nu = 1/3$ fractional quantum Hall energy gap in suspended graphene. *Phys. Rev. Lett.* **106**, 046801 (2011).
51. Dean, C. R. et al. Multicomponent fractional quantum Hall effect in graphene. *Nat. Phys.* **7**, 693–696 (2011).
52. Choi, H. C., Kang, W., Das Sarma, S., Pfeiffer, L. N. & West, K. W. Activation gaps of fractional quantum Hall effect in the second Landau level. *Phys. Rev. B* **77**, 081301 (2008).
53. Villegas Rosales, K. et al. Fractional quantum hall effect energy gaps: role of electron layer thickness. *Phys. Rev. Lett.* **127**, 056801 (2021).
54. Töke, C., Lammert, P. E., Crespi, V. H. & Jain, J. K. Fractional quantum Hall effect in graphene. *Phys. Rev. B* **74**, 235417 (2006).
55. Bolotin, K. I., Ghahari, F., Shulman, M. D., Stormer, H. L. & Kim, P. Observation of the fractional quantum Hall effect in graphene. *Nature* **462**, 196–199 (2009).
56. Li, Q. et al. Strongly coupled magneto-exciton condensates in large-angle twisted double bilayer graphene. *Nat. Commun.* **15**, 1–8 (2024).
57. Sanchez-Yamagishi, J. D. et al. Helical edge states and fractional quantum Hall effect in a graphene electron–hole bilayer. *Nat. Nanotechnol.* **12**, 118–122 (2017).
58. Wang, L. et al. One-dimensional electrical contact to a two-dimensional material. *Science* **342**, 614–617 (2013).
59. Gusynin, V. P., Miransky, V. A., Sharapov, S. G. & Shovkovy, I. A. Edge states, mass and spin gaps, and quantum Hall effect in graphene. *Phys. Rev. B* **77**, 205409 (2008).
60. Jiang, Z., Zhang, Y., Stormer, H. L. & Kim, P. Quantum Hall states near the charge-neutral Dirac point in graphene. *Phys. Rev. Lett.* **99**, 106802 (2007).
61. Giesbers, A. J. M. et al. Gap opening in the zeroth Landau level of graphene. *Phys. Rev. B* **80**, 201403 (2009).

Acknowledgements

We thank Thomas Ihn for the important discussions. J.J. acknowledges funding from SNSF. M.B. acknowledges the support of SNSF Eccellenza grant No. PCEGP2_194528, and support from the QuantERA II Program that has received funding from the European Union's Horizon 2020 research and innovation program under Grant Agreement No 101017733. K.W. and T.T. acknowledge support from the JSPS KAKENHI

(Grant Numbers 20H00354 and 23H02052) and World Premier International Research Center Initiative (WPI), MEXT, Japan.

Author contributions

J.J. and M.B. conceived the project. J.J. made all stacks and fabricated the devices. Q.G. fabricated and analyzed the data of Device_A2. J.J. performed the measurements with the help of Z.Z. J.J. has analyzed the data with inputs from C.S. and Z.Z. K.W. and T.T. provided the hBN crystals. J.J. wrote the manuscript with inputs from M.B., M.D., E.H. as well as all other authors.

Competing interests

The authors declare no competing interests.

Additional information

Supplementary information The online version contains supplementary material available at <https://doi.org/10.1038/s41467-025-56141-0>.

Correspondence and requests for materials should be addressed to Mitali Banerjee.

Peer review information *Nature Communications* thanks Rui Wang, Cheng Zhang and the other anonymous reviewers for their contribution to the peer review of this work. A peer review file is available.

Reprints and permissions information is available at <http://www.nature.com/reprints>

Publisher's note Springer Nature remains neutral with regard to jurisdictional claims in published maps and institutional affiliations.

Open Access This article is licensed under a Creative Commons Attribution-NonCommercial-NoDerivatives 4.0 International License, which permits any non-commercial use, sharing, distribution and reproduction in any medium or format, as long as you give appropriate credit to the original author(s) and the source, provide a link to the Creative Commons licence, and indicate if you modified the licensed material. You do not have permission under this licence to share adapted material derived from this article or parts of it. The images or other third party material in this article are included in the article's Creative Commons licence, unless indicated otherwise in a credit line to the material. If material is not included in the article's Creative Commons licence and your intended use is not permitted by statutory regulation or exceeds the permitted use, you will need to obtain permission directly from the copyright holder. To view a copy of this licence, visit <http://creativecommons.org/licenses/by-nc-nd/4.0/>.

© The Author(s) 2025